Materials
Advances

Accepted Manuscript

This article can be cited before page numbers have been issued, to do this please use: A. Aliabadi, M. S. Rahmanifar, B. Sohrabi, H. Aghaei and K. Zare, *Mater. Adv.*, 2025, DOI: 10.1039/D5MA00328H.

ROYAL SOCIETY
OF CHEMISTRY

rsc.li/materials-advances

View Article Online
DOI: 10.1039/D5MA00328H

Capacitive Behavior of the Electrodes Prepared by Tragacanth Gum Modified in the various Ratios and Temperatures

A. Aliabadi[a], M. S. Rahmanifar[*, b], B. Sohrabi[*, c], H. Aghaei[a], K. Zare[a]

[a] Chemistry Department, Faculty of Science, Islamic Azad University, Science and Research Branch, end of Ashrafi-Egfehani highway, Hesarak direction Tehran, Iran

[b] Faculty of basic science, Shahed University, Tehran, Iran.

[c] Department of Physical Chemistry, Faculty of Chemistry, Surface Chemistry Research Laboratory, Iran University of Science and Technology, Tehran, 16846-13114, Iran.

Proofs and Correspondence to:

Dr. Mohammad safi Rahmanifar

E-mail: rahmanf_m@yahoo.com, rahmanfm@shahed.ac.ir

Dr. Beheshteh Sohrabi
E-mail: sohrabi_b@yahoo.com, sohrabi_b@iust.ac.ir
Tel: +98-2173228315

View Article Online
DOI: 10.1039/D5MA00328H

Abstract

In the fields of energy conversion and storage, renewable, affordable, and environmentally benign electrode materials have garnered a lot of interest. Tragacanth gum (TG), a natural polymer, is recognized to have a high degree of biocompatibility; however, it is still difficult to get high conductivity. To the best of our knowledge, this study uses TG carbon precursor and $ZnCl_2$ as an active agent at 600–900 °C for 2 hours under an N_2 atmosphere, which is a simple approach for creating porous carbon materials with a high nitrogen content. The resulting TGN-3 sample has a nitrogen content of up to 1.23% weight percent and a high specific surface area of 3595.77 m^2g^{-1}. Additionally, the N-doped carbon shows good electrochemical properties (with a specific capacitance of 124.78 Fg^{-1} in 6 M KOH at the current density of 1 Ag^{-1}). Moreover, TGN-3@Ni composite was made from the sustainable carbon source TGN-3 using a straightforward hydrothermal synthesis process. As an electrode material, it demonstrated good electrochemical properties with a high rate capability and a specific capacitance of 319.9 Fg^{-1} in 6 M KOH at a current density of 5 Ag^{-1}. Then, using TGN-3 as the negative electrode, TGN-3@Ni as the positive electrode, and 6 M KOH as the electrolyte solution, an asymmetric supercapacitor (ASC) was put together. With a specific capacitance of 40.06 Fg^{-1} at 1 $Ag^{-1}$and a high energy density of 16.07 $Whkg^{-1}$ at a power density of 881.07Wkg^{-1}, this supercapacitor demonstrated good electrochemical performance. It also demonstrated exceptional cycle stability, maintaining 96.12% of its initial specific capacitance after 8000 cycles at 5 Ag^{-1}. Consequently, these experimental results confirm that the porous carbon materials with high nitrogen content can be a prospective electrode material for supercapacitors.

View Article Online
DOI: 10.1039/D5MA00328H

1. Introduction

The abundance biodegradability and biocompatibility of natural polymers provide them a clear advantage over synthetic ones. Natural gums have gained widespread attention in various features of energy, water, food, environment, biotechnology, and medicine industries due to their accessibility, structural diversity, low cost, and remarkable properties as ‘green’ bio-based renewable materials [1]. The good qualities of biopolymeric materials such as their flexibility, lightweight nature, high adsorption capacity, and consistent cycle performance have led to their recent rise in popularity for usage in supercapacitors. Furthermore, biopolymers are safer, more ecological, and more recyclable than heavy metals in battery electrodes. For usage in energy applications, these polysaccharides' inherent properties can be modified and improved. Conductive nanoparticles, such as metal nanoparticles (such as silver and gold nanoparticles), carbon-based materials, and metal oxide nanoparticles (such as zinc oxide, titanium dioxide, and iron oxide nanoparticles) can be added to improve electronic conductivity. All in all, biopolymers are now a great supply of carbon for creating porous carbon composites.

Astragalus is a shrub in Britain that secretes a natural anionic polymer called tragacanth gum (TG). Frequently utilized in food additives, thickeners, stabilizers, and hydrogels, it possesses excellent biocompatibility, biodegradability, non-toxicity, and acid resistance [2]. This natural gum is the dried exudate gathered from the stems and branches of several Astragalus species that are native to Asia's highlands but are most commonly found in northern parts of Iran. Commercial TGs from various species range significantly in chemical composition, including sugar composition, methoxy concentration, and the relative percentage of soluble and insoluble components, due to seasonal and regional fluctuations. TG is mostly a complex combination of branched acidic heteropolysaccharides that contain D-galacturonic acid. Other sugars generated

View Article Online
DOI: 10.1039/D5MA00328H

by hydrolysis include D-galactose, L-fucose (6-deoxy-L-galactose), D-xylose, and L-arabinose. Bassorin (arabinogalactan) appears to be practically neutral, with D-galacturonic acid methyl ester replacing acid units (Fig. 1a). When TG is added to water, the soluble portion, tragacanthin or tragacanthic acid, dissolves to create a viscous colloidal hydrosol, while the insoluble part, bassorin (60-70%), swells to form a gel. An aqueous solution of TG is the most viscous of all natural plant gums, and it is extremely heat stable [3]. Tragacanth gum was employed as a green binder by Scalia et al. to fabricate supercapacitors, while TG/PIL(polymer tragacanth gum and ionic liquid 1-vinyl-3- ethylimidazolium bromide) hydrogel has been employed as an electrolyte in more recent studies [4, 5]. Furthermore, it has been shown that tragacanth gum has been used in the green biosynthesis of a variety of transition metal and metal oxide nanoparticles, including ZnO-NPs [6], CuO-NPs[7], AgNPs[8] and Ag@ZnO NPs [9].Natural biomass types have recently been used as raw materials to create porous carbon materials for supercapacitors [10].

Activated carbons have been one of the most researched electrode materials in recent decades due to its inexpensive cost, abundant resources, huge surface area, adjustable porosity, and strong electroconductivity. Activated carbons are advantageous for the quick transfer of electrolyte ions in electrodes and for storing a lot of charges on the surface due to their wide surface area and improved porosity. Physical and chemical activation are the two main types of activation techniques used to prepare activated carbons. As chemical activation agents, KOH, $ZnCl_2$, and H_3PO_4 are typically employed. However, microspores predominate in activated carbons made by physical or chemical activation with KOH and H_3PO_4. Additionally, the small pore size would severely restrict the supply of electrolyte ions, which would increase resistance due to the concentration polarization effect.

View Article Online
DOI: 10.1039/D5MA00328H

This activation readily produces an adjustable porosity structure from microporous to mesoporous, in contrast to other activation techniques [11].

As the $ZnCl_2$ impregnation ratio increases, significant dehydration takes place, resulting in increased pore widening and decreased microporosity. In fact, $ZnCl_2$ has hydration and dehydroxylation effects during the activation process, which can release hydrogen and oxygen from the starting material in the form of water vapour and form a porous structure. Furthermore, $ZnCl_2$ is changed into ZnO during the activation process, which can react with carbon to break down its structure and produce a large number of pores [12], [13]. According to investigations, doping carbon materials with a specific quantity of heteroatoms (such as sulfur, phosphorus, nitrogen, etc.) can enhance their surface stability while also increasing a portion of their pseudocapacitance and raising their overall specific capacity.

In order to create a novel nitrogen-doped interconnecting porous activated carbon with high SSA from Tragacanth as a biomass precursor, we have developed a practical and effective method. Zinc chloride, a highly effective activator, was used to activate the porous carbon precursor. After being doped with heteroatom, the high-temperature nitriding process was used to swiftly and easily create nitrogen-doped activated carbon with a high SSA. Since nitrogen atom doping improves surface wettability and electrical conductivity, the results indicate that the nitrogen-doped activated carbon with high SSA has a higher charge storage capacity [14]. A distinctive nitrogen-doped activated carbon with high SSA is produced by this easy and effective synthesis procedure, and it has tremendous promise for real-world energy storage applications for high-performance supercapacitors. TG hydrogel's high conductivity is difficult to achieve, thus in this work, nickel oxide nanoparticles were also employed to alter and enhance the TG polysaccharide's inherent characteristics [14], [5].

View Article Online
DOI: 10.1039/D5MA00328H

2. Experimental section

2.1. Materials

A quantity of high-quality tragacanth (sheet) was purchased from the Tehran market. Other chemicals, nickel nitrate hexahydrate ($Ni\ (NO_3)_2\ .6H_2O$) (98.5%), urea (99%), potassium hydroxide(KOH), hydrochloric acid (HCl), zinc chloride ($ZnCl_2$), ethanol, acetylene black, poly(tetrafluoroethylene), and N-methylprolidone (NMP), were purchased from Merck and Sigma-Aldrich Chemical Companies. They were all analytical purity and used directly without further purification. Deionized (DI) water was used throughout the experiment.

.

2.2. Preparation of porous activated carbon material

Amount 2.03 g of Tragacanth powder was slowly dissolved into 200 g of water, while a mechanical stirrer was used to stir the mixture. This mixture was stirred for 3 hours at a speed of 1300 rpm to obtain a homogeneous gel of 1% (w/w); Then, it was freeze-dried to preserve the porous microstructure before and after drying.

Then the resulting material was ground with a coffee grinder and heated to a temperature of 270 °C in a tube furnace in an N_2 atmosphere at a speed of 3 $°Cmin^{-1}$ and remained at this temperature for 2 hours until it was pre-carbonized; then it was mixed with $ZnCl_2$ in different ratios of 1:1, 1:2, 1:3, and 1:4; TG/ $ZnCl_2$ w/w to be activated. Also, it was stirred for 6 hours and placed in an ultrasonic bath for 90 min. Ultimately, it was dried in an oven set at 105 °C. The resultant material was then heated to 550 °C at a speed of 5 $°Cmin^{-1}$ in a tube furnace in an N_2 atmosphere for 90 min. Next, it was heated to 800 °C at a speed of 5 $°Cmin^{-1}$, where it stayed for 2 hours until it was carbonized. The following samples were carbonized using the same procedure at 600, 700, and

View Article Online
DOI: 10.1039/D5MA00328H

900 ˚C and were designated with the symbol TG_n-m. The activation ratio with zinc chloride and temperature are denoted by the letters n and m, respectively. Finally, the special black powder was washed with a 0.1 M HCl solution to remove inorganic impurities, and it was washed several times with distilled water to reach a pH of 5-7 and then dried in an oven at 105 °C to obtain porous biomass activated carbon.

2.3. Preparation of porous N-doped activated carbon material

In order to prepare N-doped activated carbon ($TG_{1\text{-}3}$-800), urea ($CO(NH_2)_2$) was used as a nitrogen source. The $TG_{1\text{-}3}$-800 and urea samples were uniformly ground and mixed according to the mass ratio (1:1, 1:2, 1:3, 1:4; $TG_{1\text{-}3}$-800 / urea w/w), and the obtained TGN was named TGN-1, TGN-2, TGN-3, and TGN-4, respectively. Then, placed in a tube furnace under N_2 atmosphere safety. The temperature was increased to 800°C at a heating rate of 10 °C/min and held at a constant temperature of 800˚C for activation for 15 min. The boiling water was used to wash product and eliminate any extra urea decomposition products to reach a pH of 5-7. Next, the obtained product was dried at 105˚C to obtain porous nitrogen-doped activated carbon.

2.4. Hydrothermal synthesis of TGN-3@Ni composite

To prepare the TGN-3@Ni composite, dissolve 30 mg TGN-3 powder in 15mL deionized water using an ultrasonic bath with 63.9 mg $Ni(NO_3)_2 \cdot 6H_2O$. Then, 439.5 mg of urea was swiftly mixed into the solution until it was homogenous [15].

The suspension was then enclosed in 50 mL Teflon-lined stainless steel autoclaves to undergo a hydrothermal reaction at 180˚C for 16 hours. After cooling the autoclave to room temperature, the black precipitate was centrifuged, washed with distilled water and ethanol, and dried in an oven at 105˚C for 12 hours to produce the precursor TGN-3@Ni. Finally, the precursor was calcined in air at 550˚C for 90 min to produce TGN-3@Ni.

View Article Online
DOI: 10.1039/D5MA00328H

2.5. Characterization

With the support of various techniques such as scanning electron microscopy (SEM and FE SEM), transmission electron microscopy (TEM), and energy dispersive X-ray (EDX) mapping, evidence on the internal architecture, external morphology, crystallinity, and chemical composition of hollow structures can be attained. In this regard, the morphology and structure of samples were observed by scanning electron microscopy (SEM, Tescan Vega3 and FE-SEM, Tescan MIRA4), EDX (Tescan Vega2) and transmission electron microscopy (TEM, Zeiss Em10). The phase structure of the materials was characterized by X-ray powder diffraction (XRD) equipped with Rigaku Ultima IV. Raman spectra were obtained from the microscopic confocal (532 and 785 nm) Raman spectrometer. Nitrogen sorption isotherms were measured on a surface characterization analyser (Micromeritics ASAP 2020M) at 77 K. The Brunauer-Emmett-Teller (BET) technique was used to get the specific surface area, and the Barrett-Joyner-Halenda (BJH) method was used to produce the isotherms, which were then used to calculate pore size distributions. The surface functional groups of prepared TG sample were detected using Fourier Transform Infrared Spectrometry (FTIR) on a Perkin Elmer 1720-X Infrared Spectrometer. Thermogravimetric analysis was performed on a Polymer TG thermal gravimetric analyser (Mettler Toledo 851) at temperatures ranging from ambient to 800° C in presence N_2 atmosphere and air, with a heating rate of 10°C/min. The surface elemental species of the final products were evaluated by X-ray photoelectron spectroscopy (XPS, Bestec, Ea10). The working electrode was prepared blending the as-synthesized components, acetylene black and poly (tetrafluoroethylene) in mass ratios of 85%, 10%, and 5%, the mixture was dispersed in N-methyl pyrrolidone (NMP) to form slurry, this slurry then pressed onto nickel foam, each having an active mass loading of around 1.0 mg.

View Article Online
DOI: 10.1039/D5MA00328H

Using a three-electrode setup in a 6 M KOH electrolyte solution, an electrochemical test was conducted at room temperature. The Ag/AgCl electrode used as the reference electrode, the platinum sheet as the counter electrode, and the synthesized materials as the working electrodes in the three-electrode system. The Biologic SP-300 Electrochemical measurements, such as galvanostatic charge/discharge (GCD), electrochemical impedance spectroscopy (EIS), and cyclic voltammetry (CV), were performed using the kimiestate135 electrochemical workstation. The voltage ranges for the galvanostatic measurement ranged from -1.02 to 0.2 V and 0 to 0.5 V for TGN-3 and TGN-3@Ni, respectively, while the voltage ranges for the CV test ranged from -1.18 to 0.2 V and 0 to 0.56 V with various scan rates of 10–200 mVs^{-1} Electrochemical impedance spectroscopy (EIS) was performed in the frequency range from 100 kHz to 0.01 Hz.

2.6. Fabrication of the device

An asymmetric supercapacitor (ASC) was installed with TGN-3@Ni as the positive electrode, TGN-3 as the negative electrode, and 6 M KOH as the electrolyte solution in order to further explore the potential of the TGN-3@Ni composite in real-world applications.

Based on the charge balance in an ASC ($Q_+ = Q_-$) where Q_+ is the positive electrode charge, Q_- is the negative electrode charge, and $Q = (C \times m \times \Delta V)$, the mass ratio of the two electrode materials was obtained according to equation (1) [16]:

$$\frac{m_+}{m_-} = \frac{C_- \times \Delta V_-}{C_+ \times \Delta V_+} \tag{1}$$

The specific capacitances of positive and negative electrodes are denoted by C_+ and C_-, the potential windows of positive and negative electrodes by ΔV_+ and ΔV_-, and the masses of positive

View Article Online
DOI: 10.1039/D5MA00328H

and negative materials by m_+ and m_-. Base on the equation, the mass ratio of TGN-3@Ni to TGN-3 is about 0.33.

3.Results and discussion

3.1. FT-IR Analysis

The chemical makeup and functional groups of tragacanth gum were determined using Fourier transform infrared spectroscopy. Its nature as a polysaccharide is shown by distinctive peaks in the FTIR spectrum (Fig. 1b). In particular, (-O-H) stretching vibrations are responsible for the broad bands at 3274–3492 cm^{-1}, whereas (-C–H) stretching vibrations are responsible for the bands about 2919–2922 cm^{-1}. Furthermore, bands at 1373-1474 cm^{-1} are indicative of ($-CH_2$) bending vibrations, while peaks at 1650-1750 cm^{-1} show (-C=O) stretching vibrations. Between 1011 and 1026 cm^{-1}, (-C-O-) stretching vibrations are visible.

3.2. Thermal Gravimetric Analysis (TGA)

Thermal analysis has been widely used to get knowledge of the thermal behaviors of agricultural by-products.

According to the TGA curves in (Fig.1c), TG showed three steps of weight losses of about 12%, 38%, and 25% around temperatures of 150˚C, 260˚C, and 420˚C, respectively, which can be attributed to the loss of absorbed water, side groups such as acid and ester groups .Decomposition of the main chain, and the residual ash weight for pure TG at 600 °C, in a controlled nitrogen environment and exposed to air was 23.91% and 4.49%, respectively, and there was no detectable weight loss at higher temperatures. Therefore, this temperature could be the lowest carbonization temperature for the production of activated carbon from TG.

View Article Online
DOI: 10.1039/D5MA00328H

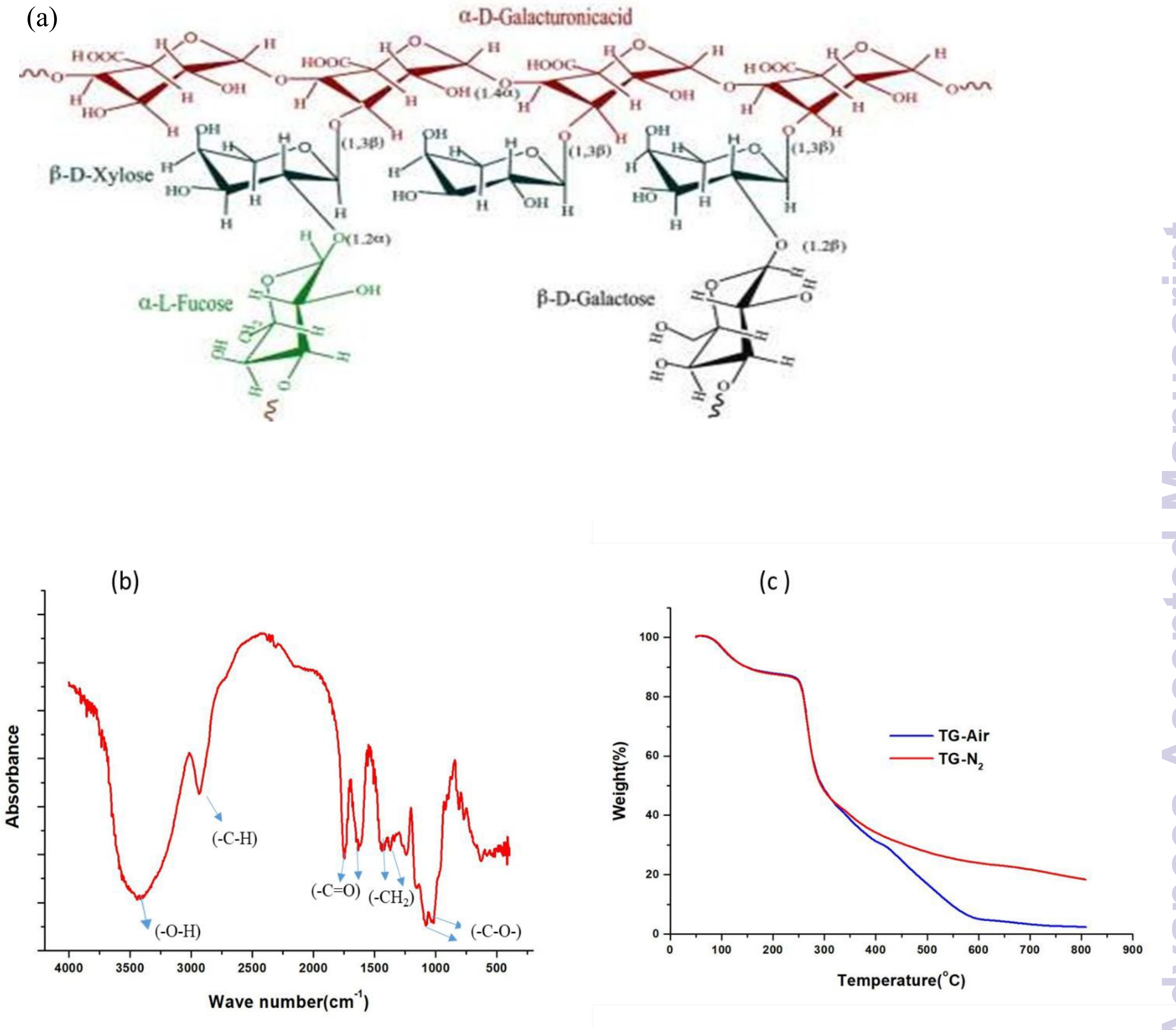

Fig. 1. (a) The structure of tragacanth gum polysaccharide. Tragacanth gum molecules are composed of sugar residues that include α-D-galacturonic acid, β-D-xylose, α-L-fucose, L-arabinose, galacturonic acid methyl ester, and β-D-galactose [3]. (b) FT-IR spectra tragacanth gum **(c)** The thermal analysis of Tragacanth gum powder in the presence N_2 atmosphere and air

View Article Online
DOI: 10.1039/D5MA00328H

3.3. Scanning Electron Microscopy (SEM)

For the transport of electrons and electrolyte ions as well as the electrochemical stability of the electrode materials, the shape of the electrode active material can produce active sites and additional penetration channels. The synthesized TG_n-m electrode material samples' SEM photos reveal that they are made up of tiny, clumped carbon microsphere particles with an uneven exterior and interstitial space, which can lead to electrolyte ion diffusion and transport.

The average diameter of carbon microspheres and the number of internal pores in the synthesised electrode materials can be increased by raising the temperature during the carbonisation process and increasing the activation ratio with $ZnCl_2$, which results in a more uniform pore distribution, according to an analysis of the SEM images (Fig. S1). The collapse of large pores on the material's surface due to excessive $ZnCl_2$ addition and temperature causes the creation of abnormally large pores. The material's initial three-dimensional pore structure is upset as a result of the smaller pores adhering to one another.

The increased number of defects in the carbon skeleton of the nitrogen-doped electrode active material results in more active sites for storing charge and the expansion of the carbon microsphere structure, which has an average diameter of around 20.96 nm and increases the electrode active material's contact area with the electrolyte (Figs. 2a and b FESEM images of the optimized electrode material TGN-3).

A large variety of chemical components as well as the distribution and dispersion of those elements inside the sample can be found using EDX analysis. The elemental mapping pictures of TGN-3 are displayed in Fig. 2 (c, d, e, and f). These pictures verify that C, O, and N are present in the TGN-3 electrode's active material. Additionally, these pictures demonstrate how evenly dispersed the O and N atoms are in the bulk carbon matrix

View Article Online
DOI: 10.1039/D5MA00328H

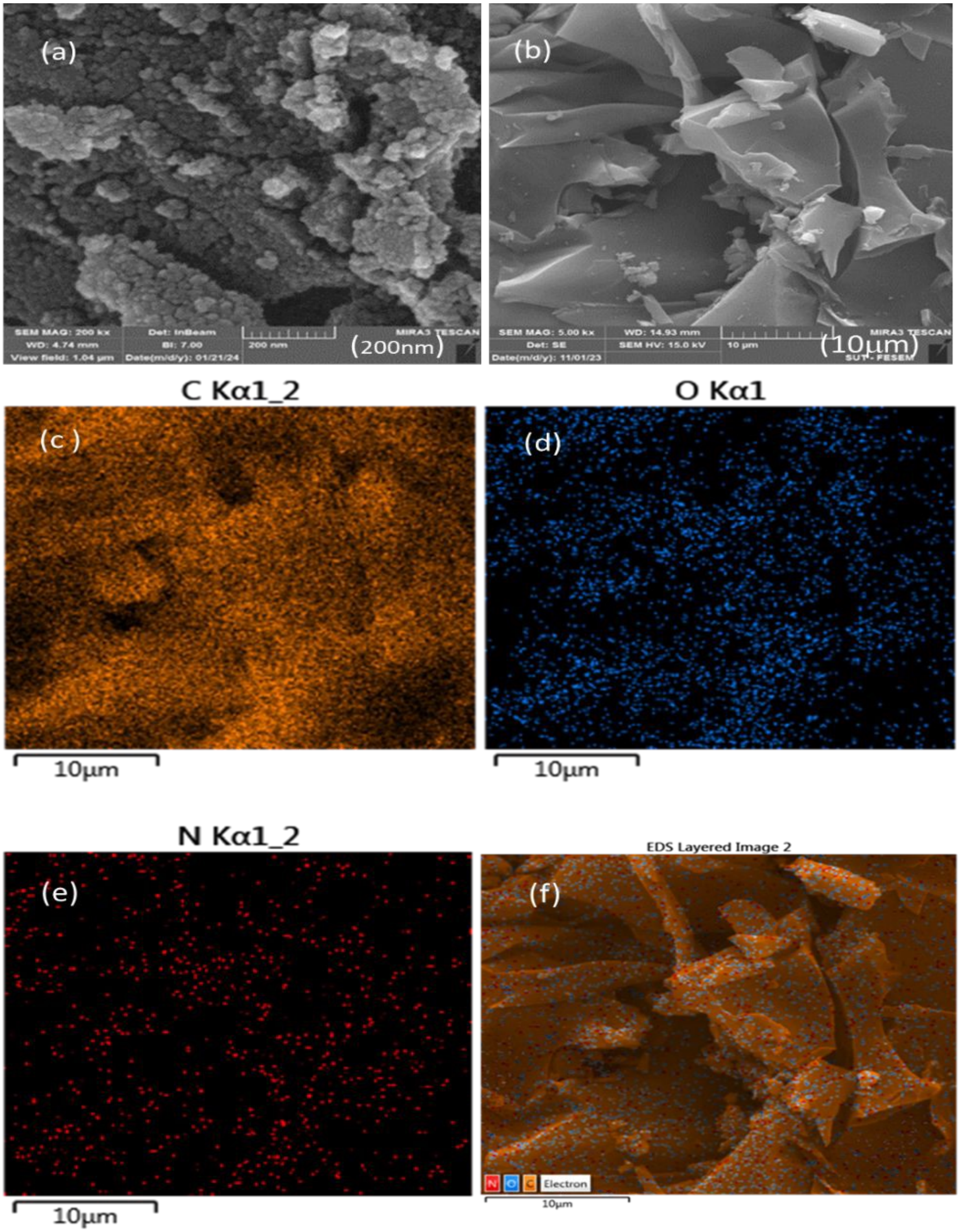

Fig.2 (a,b) FE-SEM images of $TGN\!-\!3$.(c,d,e,f) elemental mapping images $TGN\!-\!3$

View Article Online
DOI: 10.1039/D5MA00328H

One of the most popular microscopic studies for examining and studying the morphology and microstructure of materials is TEM. High-resolution TEM pictures of the TGN-3 sample are displayed in Figs. (3a and b). The presence of uniformly distributed white spots throughout the sample (shown by red dashed circles in Fig. 3a) indicates the presence of highly developed amorphous porous feature. This feature is confirmed by the XRD results and is caused by the release of gaseous contents during the carbon activation process and nitrogen doping in the TG N-3 electrode's active material[17, 18],

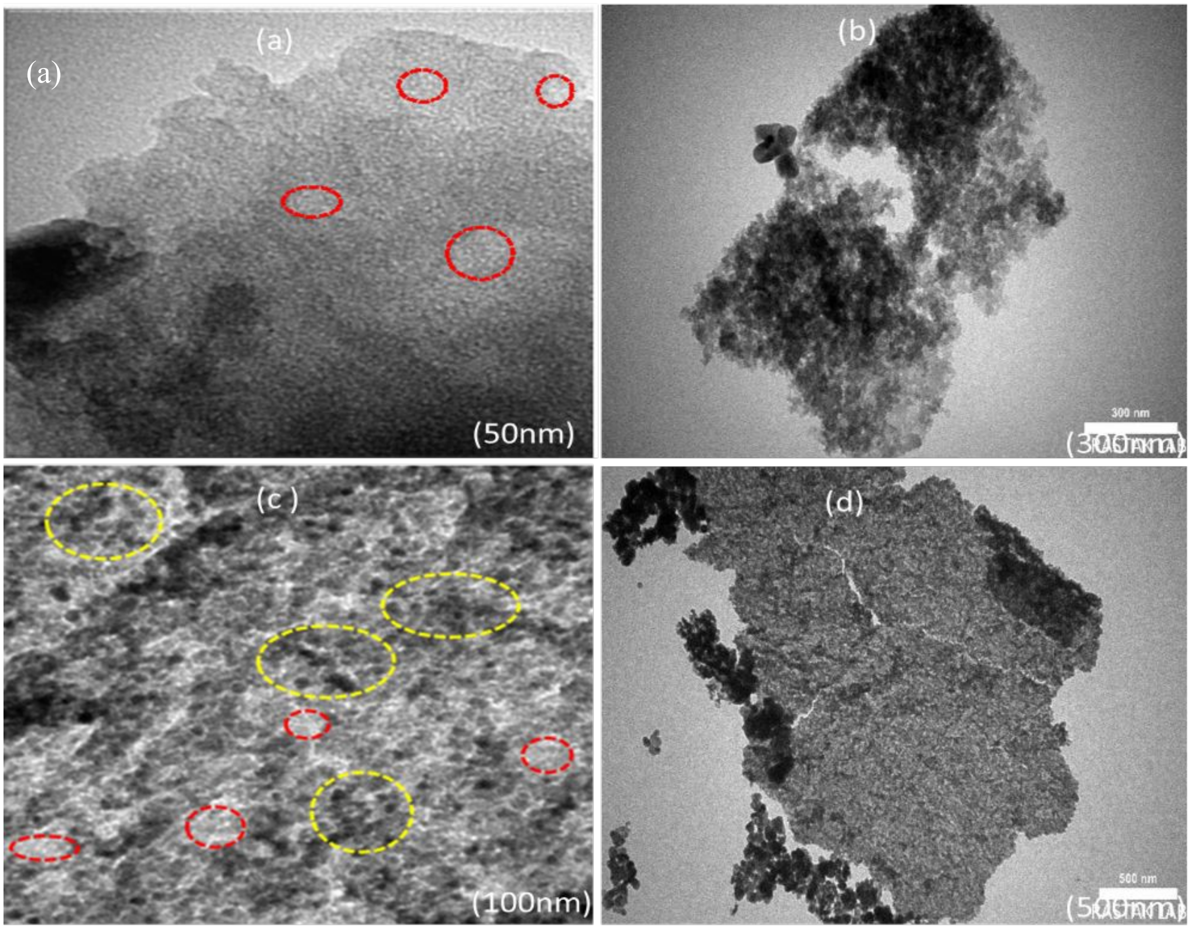

Figs.3 (a ,b) TEM (HR-TEM) micrographs for Tragacanth gum derived carbon TGN-3. (c, d) TEM micrographs of the TGN-3@Ni composite

View Article Online
DOI: 10.1039/D5MA00328H

To learn more about the microstructure of the TGN-3@Ni composite, TEM research was done. The nickel oxide nanoparticles in the TGN-3@Ni composite are uniformly embedded in the TGN-3 carbon matrix, as demonstrated by the high-resolution TEM images (Figs. 3c and 3d). Their monodisperse nature is evident in the figure, and the yellow and red circles in Fig. 3c stand for nickel oxide nanoparticles and carbon thin layers, respectively. While the carbon layers are anticipated to enhance electrical conductivity and the metal oxide nanoparticles offer more active sites, the pores in the composite may result in an increase in specific surface area. Consequently, a sizable electroactive surface with excellent electrochemical performance is produced without any appreciable NiO nanoparticle aggregation [19, 20].

3.4. BET Specific Surface Area and Pore Size Analysis

BET analysis was carried out to determine the precise surface area, diameter, volume, and pore size distribution of the synthesized electrode active materials. Table (1) provides a summary of the BET surface area, pore size distribution, and pore volume parameters of the porous carbon in the samples of synthetic electrode active materials. The BET method was used to get the total surface area in Table (1), the t-plot method was used to determine the micropore surface area and volume, and the Barrett–Joyner–Halenda (BJH) method was used to determine the total pore volume and average pore diameter based on the desorption.

View Article Online
DOI: 10.1039/D5MA00328H

Table 1. Total Surface area calculated using the BET method Micro pore Surface area and volume calculated from t-plot method Total pore volume calculated at p/p0=0.97. Average pore diameter calculated from BJH desorption

Sample name	BET Surface Area m^2g^{-1}	t-plot External Surface Area m^2g^{-1}	t-plot micrOpore Area m^2g^{-1}	t-plot micrOpore volume cm^3g^{-1}	BJH desorption average pore with (nm)	Total pore volume at p/p_0=0.97 cm^3g^{-1}	V_{mi}/V_t (%)
$TG_{1-1}-800$	890.08	141.89	748.19	0.348	3.532	0.442	78.73
$TG_{1-2}-800$	1702.12	571.00	1131.11	0.519	5.015	1.123	46.21
$TG_{1-3}-800$	4302.83	2776.88	1525.95	0.664	4.300	2.1	31.61
TGN-3	3595.77	2850.29	745.48	0.293	3.928	1.67	17.54
$TG_{1-3}-600$	2362.25	1617.98	744.26	0.308	2.632	1.186	25.96
$TG_{1-3}-700$	2236.99	1621.14	615.84	0.252	2.673	1.156	21.79
$TG_{1-3}-900$	1931.77	1645.10	286.67	0.110	3.197	1.488	7.39
$TG_{1-4}-800$	4760.24	8025.33	-	-2.05	4.05	5.12	-

Since the use of porous carbon materials requires a pore size distribution, nitrogen adsorption and desorption experiments were used to assess the samples' specific surface area and pore structure. Micropores, mesopores, or macropores can coexist in the TG_{1-3}-800, as shown in Fig. 4a, according to a mixed I/IV type isotherm with very steep uptakes at low relative pressure (P/P_0) and a typical hysteresis loop extending P/P_0 from 0.4 to 1.0 [21].

The TGN-3 sample exhibits adsorption behavior that is more akin to the type I adsorption curve; the micropore filling effect causes the adsorption content to increase sharply in the low relative range, followed by multilayer sorption and capillary condensation at higher pressure. Furthermore, the presence of macropores is indicated by the increasing trend of the isotherms' tails at relative

View Article Online
DOI: 10.1039/D5MA00328H

pressures around unity. It is evident from this that TGN-3 has a considerable number of macropores, mesopores, and micropores [22].

A greater specific surface area is attained as a result of the production of more pores, as evidenced by the flat plateau of the isotherms in Fig. 4a moving to a higher position when the activation temperatures rise from 600 °C to 800 °C [23].

For the process of charge storage, a large specific surface area (SSA) can offer a large number of electrochemical active sites. Shortening the electrolyte ion diffusion route can be achieved by increasing the SSA due to the porous structure and exposition of the interior material for improved contact with the electrolyte. Thus, SSA and porous structure are important variables affecting the electrode material's capacitance performance [22]. Conversely, when the activation temperature is raised to 900 °C, the plateau shifts downward and some of the micropore and mesopore structure collapses (Fig. 4a). Thus, the micropore volume dropped to 0.11 cm^3g^{-1} and the specific surface area dropped to 1931.77 m^2g^{-1} [23]. As shown in Fig.4b, both the TG_{1-1}-800 and the TG_{1-2}-800 exhibit distinct plateaus in the low-pressure range, suggesting that there are a sizable number of micropores present. A type II isotherm with steep adsorption is displayed by the TG_{1-4}-800 sample, where micropores were destroyed by additional activation [21].

TG_{1-3}-600, TG_{1-3}-700, TG_{1-3}-800, and TG_{1-1}-800 samples have type H4 weak hysteresis loops according to the IUPAC classification of hysteresis loops for desorption isotherms, whereas TG_{1-2}-800 sample exhibits a transit from type H_4 to H3 hysteresis loops. Furthermore, it is clear that TG_{1-2}-800 has an apparent hysteresis loop, indicating inadequate pore openness and a rough pore wall in the absence of sufficient activation of $ZnCl_2$ [24]. While type H4 hysteresis loops are always found in materials with narrow slit-shaped pores that contain both micropores and mesopores, type H3 and H4 hysteresis loops are linked to slit-shaped pores [25]. Using the BJH theory, the pore size distribution (Fig. 4c) was computed from the desorption branch of the isotherm. Table 1 shows how the mass ratio of TG/$ZnCl_2$ affects the textural development of the TG-derived carbon porosity properties at various ratios of 1:1, 1:2, 1:3, and 1:4. The growth of porosity, particularly at the mesopore level, is significantly influenced by the activation ratio. As the activation ratio increased, the BET surface area, total pore volume, average pore diameter, and exterior surface area of the $TG_n - 800$ samples all exhibited an upward trend until the impregnation ratio reached 1:3. Since the impact of $ZnCl_2$ inhibits tar formation and promotes volatile release at low impregnation ratios, more micropores are created. However, a larger impregnation ratio will cause the pores to inflate further into the impregnated precursor material and release more volatiles during the carbonisation process. The resulting micropores will then become mesopores [26].

However, the $TG_{1\text{-}4}$-800 sample had no micropore surface area or volume when the activation ratio was adjusted to 1:4. This is to be anticipated since many nearby micropores may collapse or create mesopores and macropores. Thus, the ideal impregnation ratio was determined to be 1:3. because the EDLC capacity might be efficiently increased by microporous charge storage [27].

Fig. 4d displays the range of pore size based on N_2 desorption data in the $TG_{1-3} - m$ at temperatures ranging from 600 to $900^{\circ}C$. Samples $TG_{1\text{-}3}$-600 through $TG_{1\text{-}3}$-900 have specific surface areas of 2365.25, 2236.99, 4302.83, and 1931.77 m^2g^{-1}, respectively, and total pore volumes of 1.186, 1.156, 2.100, and 1.488 cm^3g^{-1}, respectively. When the activation temperature was increased to $800^{\circ}C$, more holes were formed, and the specific surface area increased to 4302.83 m^2g^{-1}. The creation of some micropores and their linking to generate mesopores caused the micropore volume fraction to decrease to 31.61%. However, a fall in the volume fraction of

View Article Online
DOI: 10.1039/D5MA00328H

micropores to 7.39% occurs when the activation temperature is raised to 900°C, which results in the collapse (or sintering of the small pore walls) of a portion of the micro- and mesopore structure. Consequently, the total pore volume drops from 2.1 to 1.48 cm^3g^{-1}, and the specific surface area drops from 4302.83 to 1931.77 m^2g^{-1}. It is evident that capacitance increases with specific surface area, and as a result, the produced sample exhibits superior chemical performance. Thus, 800°C is chosen as the ideal carbonization temperature for making activated carbon from the TG biopolymer process. The pore size distribution reveals that the volume of mesopores in the TG_{1-3}-800 and TGN-3 samples increases from 68.38% to 82.45%, respectively, and the specific surface area decreases from 4302.83 m^2g^{-1} in the TG_{1-3}-800 sample to 3595.77 m^2g^{-1} in the TGN-3 sample when the TG sample is doped with nitrogen, as shown in Table 1. The volume fraction micropores drop to 17.54% from 31.61%. The initial regular structure is likely to be distorted as a result of the mesopores expanding in a particular direction due to the increased amount of nitrogen functional groups on the carbon surface [25]. This is confirmed by the XRD diffraction measurements. More active areas for charge storage may be available due to the severely flawed structure.[28].

The quick filling of small pores with electrolyte is thus made possible by TGN-3, which has a large specific surface area and a more significant pore size. These mesopores serve as conduits for rapid electrolyte transport and diffusion. The TGN-3 electrode active material seems to have a greater specific capacity and rate of operation, according to the results of N_2 adsorption-desorption and pore size distribution[29].

View Article Online
DOI: 10.1039/D5MA00328H

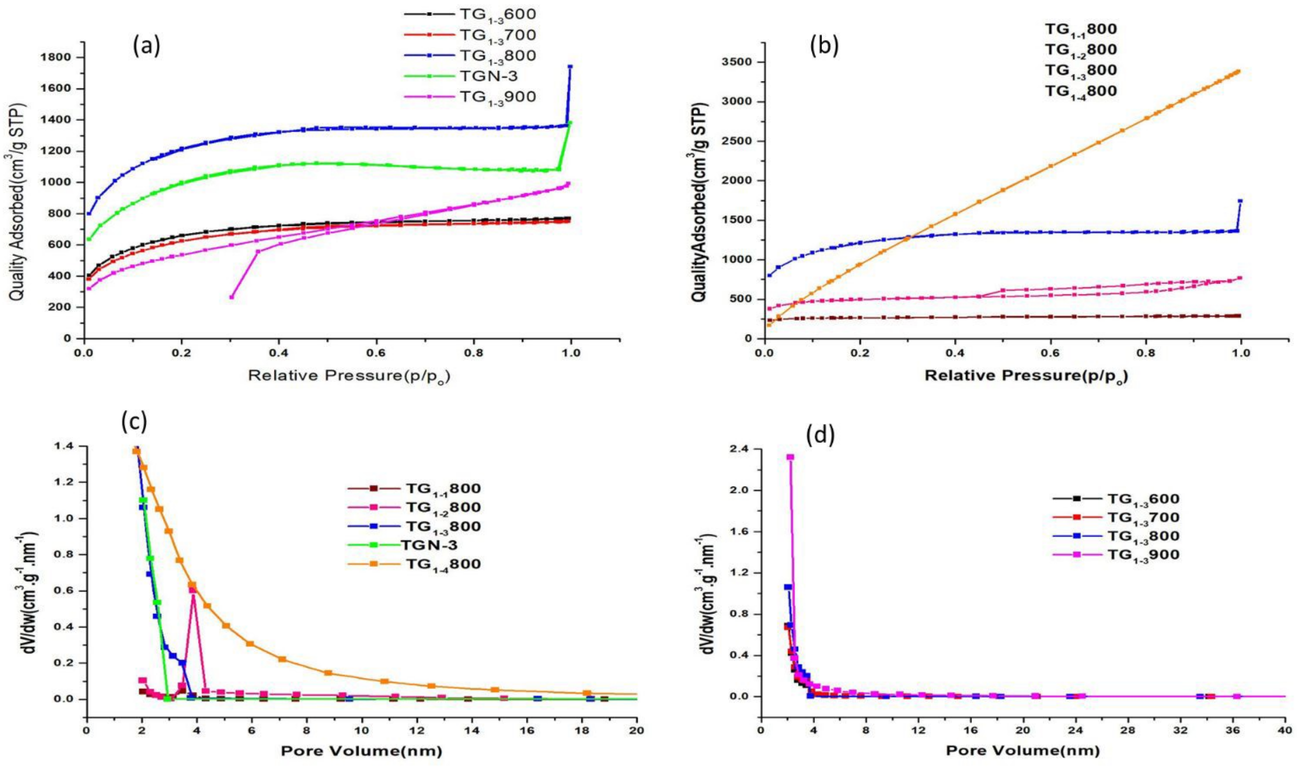

Fig.4. Adsorption and desorption isotherms of activated TG/$ZnCl_2$ (a) with a 1:3 ratio at temperatures of 600 ℃, 700 ℃, 800 ℃ ,900 ℃ and TGN-3 (b) with ratios of 1:1 to 1:4 at temperature 800℃ (c) Pore size distribution measured for TG_{1-1}-800, TG_{1-2}-800, TG_{1-3}-800 , TG_{1-4}-800 and $TGN-3$ based on N_2 desorption data (d) Pore size distribution measured for TG_{1-3}-600, TG_{1-3}-700, TG_{1-3}-800 and TG_{1-3}-900 based on N_2 desorption data.
.

3.5. XRD Analysis

The phase structure of samples was characterized by XRD. The XRD patterns of TG_n -m ,TGN-3 and TGN-3@Ni materials are shown in Fig.5. All the patterns exhibited two broad XRD peaks between 22 & 30 and 42 & 45, to the (002) interlayer spacing between adjacent graphite layers and (100) in-plane ordering of graphite, respectively [30].

Remarkably, when the impregnation ratio of the samples in activation with $ZnCl_2$ (Fig. 5a) and the carbonization temperature increase (Fig. 5b), the diffraction peak (002) of the samples

View Article Online
DOI: 10.1039/D5MA00328H

decreased significantly and became wider and at the same time the intensity of the plane (100) also decreased and during the N-doping process of the TGN-3 sample (Fig. 5a), the carbon network becomes more and more disordered [20]. These points indicate that a large number of amorphous structures are formed due to the presence abundant density of pores in TGN-3 sample with a high specific surface area [31], [32].

The diffraction peaks at the (2θ) angles of 37.24, 43.36, 63.0, 75.44, and 79.56, which correspond to the (111), (200), (220), (311), and (222) planes of the cubic NiO (JCPDS No. 47.1049), provide additional evidence for the presence of NiO and further analysis of the crystal structure of the TGN-3@Ni composite (Fig. 5c). Furthermore, the high crystallinity of the TGN-3@Ni composite is shown by the existence of substantial diffraction peak intensities [33].

3.6. Raman spectroscopy Analysis

To comprehend the structural development of the modified carbon activated at various temperatures, Raman scattering measurements were performed. Raman spectra (Figs. 5d and 5e) reveal the graphitization quality of the TG_n -m materials.

All the TG_n -m materials exhibit two characteristic peaks; a D-band (near 1336 Cm^{-1}) and G-band (near 1592 Cm^{-1}), representing the disordered and graphitic nature respectively. The graphitic band is closely associated with the vibrations of sp^2 -bonded carbon atoms in the 2d hexagonal lattice, while the defect peak arises due to sp^3 -hybridized carbon [34].

The intensity ratio of the D to G band (ID/IG) can reflect the graphitization degree of carbon materials [35]. The calculated ID/IG values of TG_{1-3} -600, TG_{1-3} -700, TG_{1-3} -900 , TG_{1-1} -800, TG_{1-2} -

View Article Online
DOI: 10.1039/D5MA00328H

800, TG_{1-3}-800, TG_{1-4}-800, and TGN-3 are 0.767, 0.900, 0.936, 0.840, 0.880, 0.866, 0.938, and 0.923, respectively.

The increase in regular carbon content at 800 $^{\circ}C$ temperature shows that not only more holes based on SEM and TEM data are created after the activation process, but also the degree of graphitization increases. The sample activated at 600 $^{\circ}C$ has the maximum degree of graphitization, but graphitization diminishes as the activation temperature rises. Also, the results show that the N-doping and $ZnCl_2$ activation can provide more structural defects, leading to higher degree of disorder [28].

The equivalent series resistance of supercapacitors should decrease as a result of the enhanced electric conductivity caused by the enhanced graphite degree of activated carbon. [36].

View Article Online
DOI: 10.1039/D5MA00328H

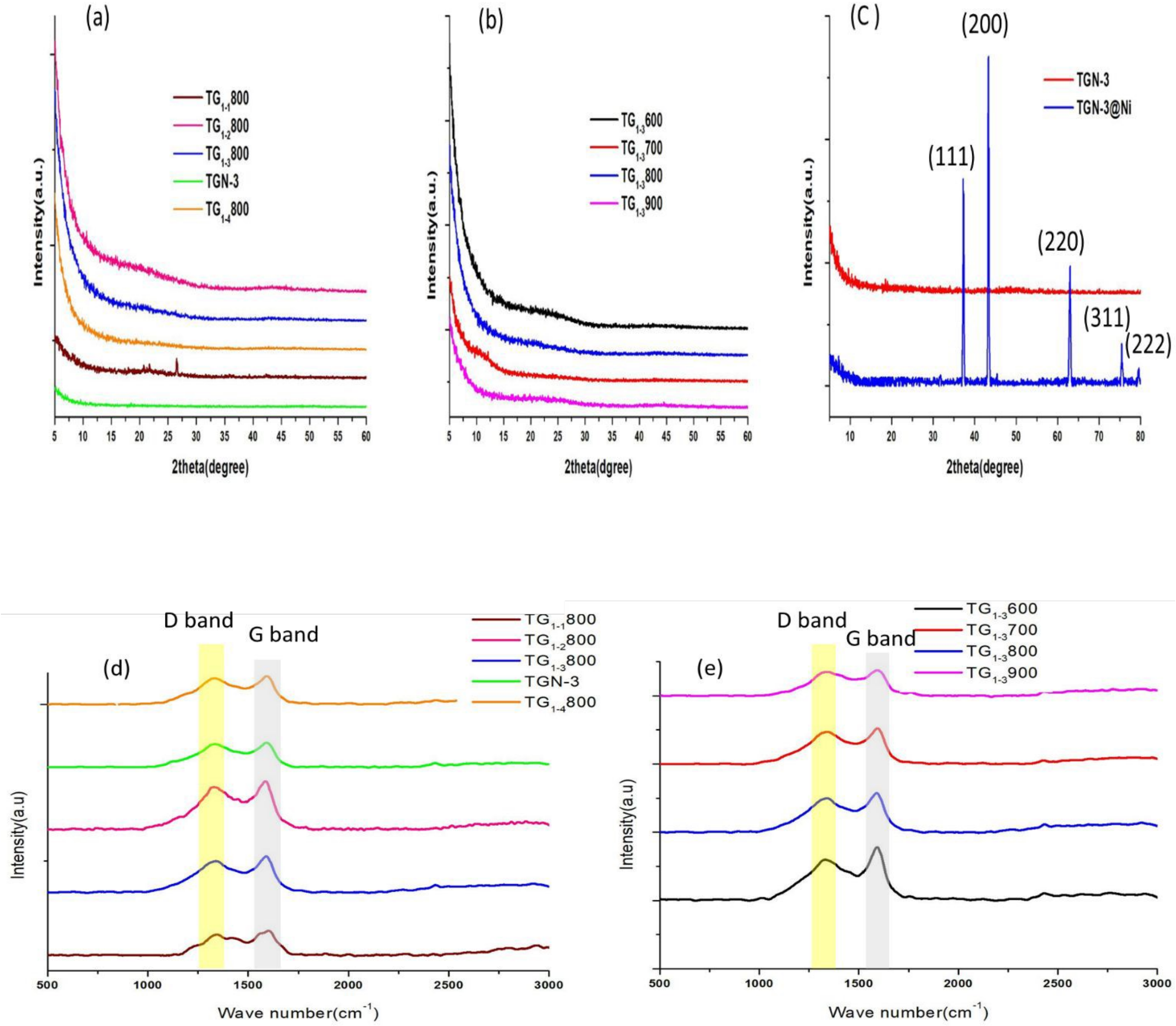

Fig.5. XRD patterns for activated TG (a) with ratios of 1:1 to 1:4 and TGN-3 at temperature 800℃ (b) with a 1:3 ratio at temperatures of 600℃, 700℃, 800℃ and 900℃. XRD pattern of the TGN-3@Ni composite(c). Raman spectra of the activated TG (d) with ratios of 1:1 to 1:4 and TGN-3 at temperature 800℃ (e) with a 1:3 ratio at temperatures of 600℃, 700℃, 800℃, and 900℃

View Article Online
DOI: 10.1039/D5MA00328H

3.7. XPS Analysis

X-ray photoelectron spectroscopy (XPS) is used to examine the elemental composition, chemical states, and N doping in activated carbon. As shown in Fig. 6a, the survey spectra of the samples contain N, O, C, and Ni atoms.

Fig. 6b shows the XPS spectrum of TGN-3. Three prominent peaks around 285 eV, 400 eV, and 533 eV correspond to the 1s peaks of carbon, nitrogen, and oxygen, respectively. The peak at 285 eV verifies the presence of amorphous carbon [16].

The TGN-3 sample's high-resolution C 1s spectra (Fig. 6c) identified three peaks: C=C (284.2 eV), C-C/C=N (~285.2 eV), and O-C=O (288.8 eV) [37,38, 39].

Furthermore, the nitrogen dopant profiles showed two primary peaks at about 400.2 and 398.3 eV (Fig. 6d), corresponding to pyrrolic N (N-5) and pyridinic N (N-6), respectively. Exceptional electron donor capabilities and charge transfer rate created by pyrrolic-N and pyridinic-N might greatly enhance the activity of the electron transfer process [20]. The results of XPS indicate that mass ratio of nitrogen in the treated activated carbon is 1.23%.

The O 1s spectra revealed two peaks with binding energies of 530.1 and 531.8 eV, representing C=O groups (O-I) /Ni-O band and C-OH /C-O-C groups (O-II), respectively [40].

Fig. 6e shows that TGN-3 has more O-II, which can react with OH^- in an alkaline electrolyte to give pseudo capacitance. As a result, carbon-based materials containing O- and N-based functional groups might generate reversible faradaic processes and give pseudo capacitance. These O- and N-based functional groups may also improve the electrical conductivity and wettability of porous carbons [41].

View Article Online
DOI: 10.1039/D5MA00328H

Ni $2p_{1/2}$ and Ni $2p_{3/2}$ are identified by the peaks in the XPS spectra of Ni 2p (Fig. 6f) that are centered at 872.6 eV and 855 eV, respectively. Each of these peaks has a shakeup satellite peak at a higher binding energy of about 6.0 eV. A feature of Ni2p in NiO of the composite is the spin energy separation between Ni $2p_{1/2}$ and Ni $2p_{3/2}$ peaks which is approximately 18 eV [42].

View Article Online
DOI: 10.1039/D5MA00328H

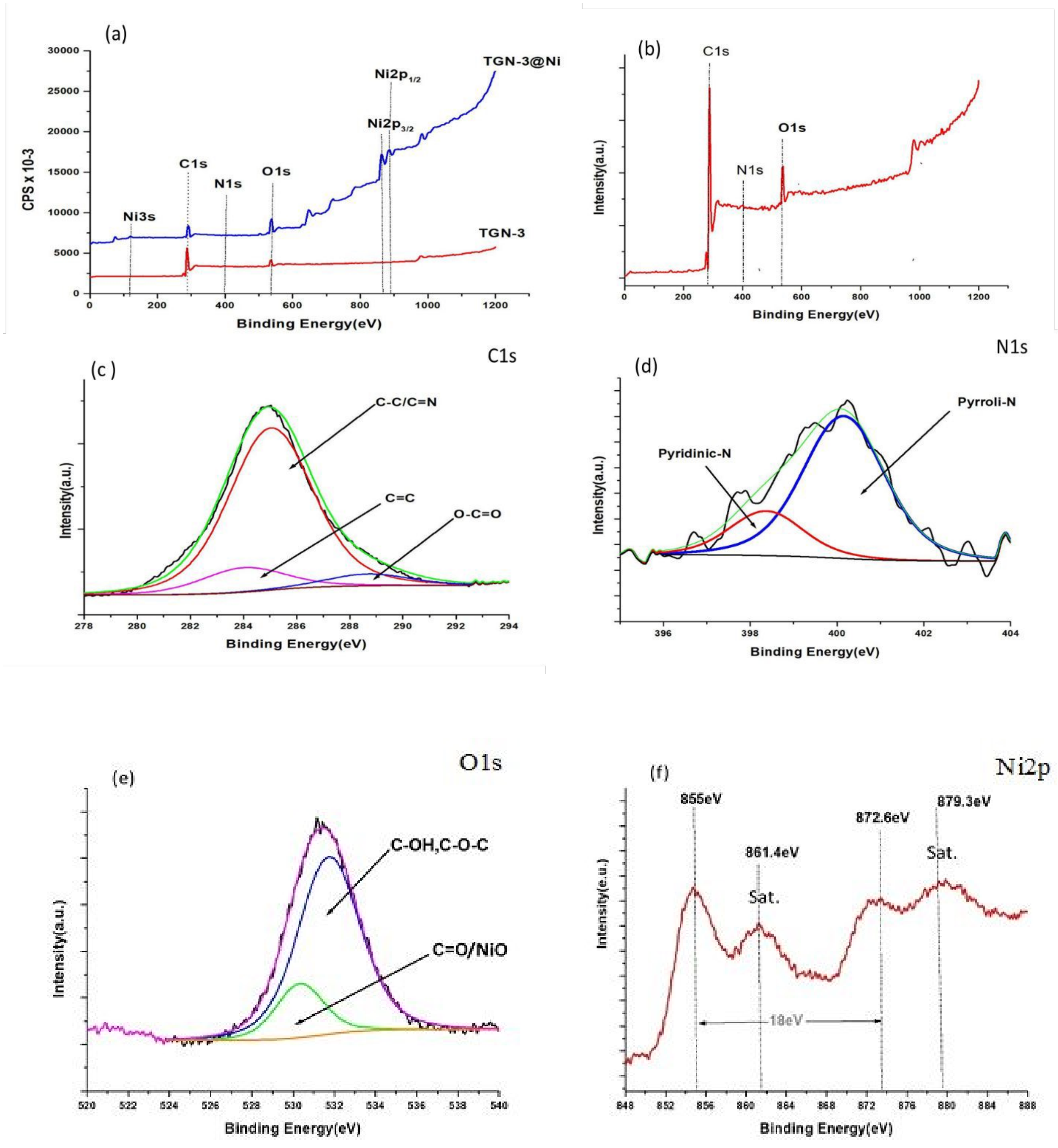

Fig.6 (a) XPS survey spectra of TGN-3@Ni and TGN-3. XPS spectrum of (b) TGN-3; (c) C1s; (d) N1s and (e) O1s (f) Ni 2p, XPS spectra of composite TGN-3@ Ni

View Article Online
DOI: 10.1039/D5MA00328H

3.8. Electrochemical Performance Analysis (Three- Electrode System)

We used a three-electrode setup to analyze all carbon material samples in 6 M KOH electrolytes. Carbons' electrochemical behavior was estimated using cyclic voltammetry (CV). CV curves of TG_{1-3}-600, TG_{1-3}-700, TG_{1-3}-800, and TG_{1-3}-900 measured at a scan rate of $50\,mVs^{-1}$ are shown in Fig. 7a.

TG_{1-1}-800, TG_{1-2}-800, TG_{1-3}-800, and TG_{1-4}-800 activation CV curves at various ratios with $ZnCl_2$ in a scan rate of $50\,mVs^{-1}$ are shown in Fig. 7b, while Fig. 7c displays TGN-1, TGN-2, TGN-3, and TGN-4 CV curves with respect to various N-doping ratios in the voltage ranges (-1.18 to 0.2V) and have been measured at a scanning speed of $50\,mVs^{-1}$.

The CV curves of these porous materials showed rectangular forms with a small distortion, as seen in Figs.7a and 7b. This behavior was characteristic of the almost perfect EDLC that was based on ionic adsorption and desorption. The nearly rectangular CV curves in Fig.7c also showed that these carbon materials, which are porous as electrode materials, had good rapid charge and discharge features. However, the double-layer and Faradaic (pseudocapacitive) charge storage mechanisms between the active materials and electrolyte, which were induced by nitrogenous groups, overlapped, slightly distorting the CV curves [43], [44].

In contrast to the EDLC mechanism, the pseudocapacitive behavior is typically accompanied by a high specific capacitance and a comparatively high energy density. This is because, in contrast to EDLC, where ion adsorption only occurs at the surface layers, the bulk of the material is exposed to redox processes [45].

The material's specific capacitance is reflected in the cyclic voltammetric area. Because of its high specific surface area (up to 3595.77 m^2/g) and suitable nitrogen concentration (1.23 %), the TGN-

View Article Online
DOI: 10.1039/D5MA00328H

3 sample had the biggest CV curve area when compared to other samples, confirming that it had the highest specific capacitance (Table 2) [43].

Fig. 7d displays sample TGN-3's CV curve at various scan rate ranging from 10 to 200 mVs^{-1}. The CV curves' area steadily grows as the sweep speed rises while maintaining a nearly constant shape, suggesting that the TGN-3 material possesses superior charge propagation and quick ion transport [35]

The specific gravimetric capacitances (C, Fg^{-1}) were calculated from the CV curves according to equation (2):

$$C = \frac{A}{2v\Delta Vm} \tag{2}$$

Where A is area under the CV curve (mAV), v is scan rate (mVs^{-1}), ΔV is potential window (V) and m is mass of working electrode (g) [46].

Table 2 shows the specific capacitance data of these electrodes. These values are smaller than the value reported for TGN-3.

Table2: Specific capacitance (Fg^{-1}) Electrode carbon material at scan rate 50 (mV/s)

Electrode material	Specific capacitance (Fg^{-1})at scan rate 50(mV/s)
TG_{1-1} -800	1.87
TG_{1-2} -800	6.55
TG_{1-3} -800	27.83
TG_{1-3} -600	15.94
TG_{1-3} -700	7.75
TG_{1-3} -900	12.27
TG_{1-4} -800	21.18
TGN-1	32.17
TGN-2	46.38
TGN-3	79.57
TGN-4	51.52

View Article Online
DOI: 10.1039/D5MA00328H

The study mentioned above shows that TGN-3 has high specific capacitances and good rate capability, which are mostly due to the following factors:

(1) The N-atom doping, such as N-6 and N-5 doping effectively providing the Faraday effect to improve the performance of supercapacitors [47]; (2) the generation of pseudo capacitance can increase the capacity of the capacitor through the attraction of the N atom in the carbon material; and (3) The charge storage within microporosity is strengthened by the abundance of active sites that are generated in situ at the pores of nitrogen-doped porous carbons with permeable defect-related porosity which can quickly contact the electrolyte and increase the capacity of the double-layer capacitor [29].

Galvanostatic charge-discharge (GCD) tests were conducted across a potential range of -1.02 to 0.2 V in order to validate the electrochemical characteristics of TGN-3. The GCD curves recorded at different applied currents of 1, 2, and 5 Ag^{-1} are displayed in Fig.7e. Additionally, because the electrolyte ions have enough time to enter and diffuse into the porosity at lower current densities, the charge-discharge time significantly lowers as the current density increases. In other words, the TGN-3 sample shows the maximum charge-discharge duration at a current density of 1 Ag^{-1}.

Like the CV curve data, the GCD results confirm that the TGN-3 sample has the best capacitive performance and exhibits the capacitive behavior. TGN-3@Ni composite was created in this work using a hydrothermal process and calcination. XPS, XRD and TEM results showed that the precursor (TGN-3) had successfully transformed into TGN-3@Ni. TGN-3@Ni's electrochemical performance was initially assessed using a three-electrode setup in a 6 M KOH solution. The TGN-3@Ni electrode's CV curves at various scan rates are displayed in Fig. 7f. The TGN-3@Ni electrode exhibits advantageous pseudocapacitive behavior with reversible Faradic charge storage,

View Article Online
DOI: 10.1039/D5MA00328H

as evidenced by the integral area of the CV curves growing bigger and the shape remaining constant as the scan rate increases [33].

The CV curves showed a distinct pair of redox peaks, one of which is anodic during the oxidation reaction of Ni^{2+} to $Ni^{3+}$and the other is cathodic during the reverse process. This suggests that the faradaic reaction is primarily responsible for the capacitance properties [48].

$$NiO + OH^{-} \leftrightarrow \quad NiOOH + e^{-}$$

Due to an increase in internal diffusion resistance within the electrod active material, the current rose as the scan rate increased, causing the oxidation peaks to shift to a more positive position and the reduction peaks to shift to a more negative position [49].

As seen in Fig7.g, the capacitance property was determined using galvanostatic charge-discharge throughout a potential range of 0–0.5 V with increasing current density from 1 to 40 Ag^{-1}. All GCD curves had symmetrical forms, indicating a reversible redox reaction of the TGN-3@Ni electrode with notable pseudocapacitance performance [33, 41]. The specific capacitance of a single electrode (C_s, Fg^{-1}) for the three-electrode system was calculated from the discharge curves according to the following equation (3) [50]:

$$C_S = \frac{I.\Delta t}{m.\Delta V} \tag{3}$$

where I is the discharge current (A), Δt (s) is the discharge time, m (g) is the mass of the active material of the individual electrode, and ΔV (V) is the voltage range.

Specific capacitances of the TGN-3@Ni electrode material were measured using the discharge curves 319.5, 292.4, 260.8, 237, and 215 Fg^{-1} at 5, 10, 20, 30, and 40 Ag^{-1}, respectively, Furthermore, increasing the current density to 40 Ag^{-1} resulted in 67.2% of the original capacity remaining. Capacitance retention at such high current density is due to the advantages of the TGN-3@Ni composite. This might be ascribed to the large specific surface area and higher conductivity

View Article Online
DOI: 10.1039/D5MA00328H

of Tragacanth-derived porous carbon containing NiO and N. The large surface area of porous carbon allows for large numbers of superficial electroactive species to participate in faradic redox reactions. Furthermore, the active material's enhanced conductivity will create a conduit for electron transport, allowing for faster charging and discharging. As a result, integrating these two materials into a single electrode enhanced the electrochemical characteristics for supercapacitor applications [40].

Table 3. Comparison of the Present Work with the Literature on NiO/Carbon Composites

Electrode material	Specific capacitance (F g^{-1})	Potential window (V vs. ref. electrode	Rate capability in % retention (current density range)	Stability in % retention (number of cycles)	Electrolyte	Ref.
NiO@SW-CFs	356 at 2 A g^{-1}	0.1–0.6 (V vs. Hg/ HgO)	40% (2–30 A g^{-1})	93% ,10Ag^{-1} (5000cycles)	2 M KOH	[51]
NiO@AMCRs	858 at 3 A g^{-1}	0–0.45 (V vs. SCE)	54% (3–50 A g^{-1})	66% ,10 Ag^{-1} (10 000 cycles)	2 MKOH	[51]
CNF/NiO	674 at 0.5 A g^{-1}	0-0.6(V vs. Hg/ HgO)	63% (0.5–10 A g^{-1})	98.6%, 0.5 Ag^{-1} (5000 cycles)	6 M KOH	[20]
NiO/NCHS composite	585 at 1A g^{-1}	0−0.5(V vs Ag/AgCl)	50.4%(1-10 A g^{-1})	115%, 5Ag^{-1} (6000 cycles)	2 M KOH	[42]
NC/Ni@NiO	390 at 2A g^{-1}	0−0.4 (V vs SCE)	59.4%(1-10 A g^{-1})	70.2%, 2Ag^{-1} (5000cycle)	6 M KOH	[52]
3D flower-like nickel oxide/ nickel composites	363.7 0.5 A g^{-1}	0–0.5 (V vs. Hg/HgO)	63.7 %(1-8 A g^{-1})	89%, 1 A g^{-1} (1000cycle)	6 M KOH	[53]
NSCDC/NiO	804 at 1 A g^{-1}	-0.4-0.8v -----	53.48 %(1-10 A g^{-1})	73.2%,5 A g^{-1} (5000cycle)	3M KOH	[54]
SDCC-NiO	23.25 at 1 A g-1	0-0.6 (V vs SCE)	36.68%(5-15Ag^{-1})	------	1M KOH	[46]
PC-NiO	811.46 at 1 A g^{-1}	0−0.5 (V vs Ag/AgCl)	-----	95.25%,1Ag^{-1} (1000cycle)	6 M KOH	[55]
Ce/Ni composite	268 at 0.2 A g^{-1}	-1.0 -0 (V vs SCE)	74.2%(0.2-2Ag^{-1})	97% ,0.2 Ag^{-1} (2000cycle)	6 M KOH	[56]
TGN-3@Ni	319.5 at 5Ag^{-1}	0−0.5 (V vs Ag/AgCl)	67.29%(5-40Ag^{-1})	96.12%,5Ag^{-1} 8000cycle(ASC)	6 M KOH	This work

This study's electrochemical results are compared to prior recent findings on NiO/carbon with diverse configurations, as shown in Table 3.

View Article Online
DOI: 10.1039/D5MA00328H

The high specific capacitance of the TGN-3 @Ni nanocomposite is superior or comparable to most of the recently reported NiO-based electrode materials. Given the above, the as-prepared TGN-3@Ni, which has outstanding electrochemical characteristics, is a viable choice for the positive electrode active material in supercapacitors.

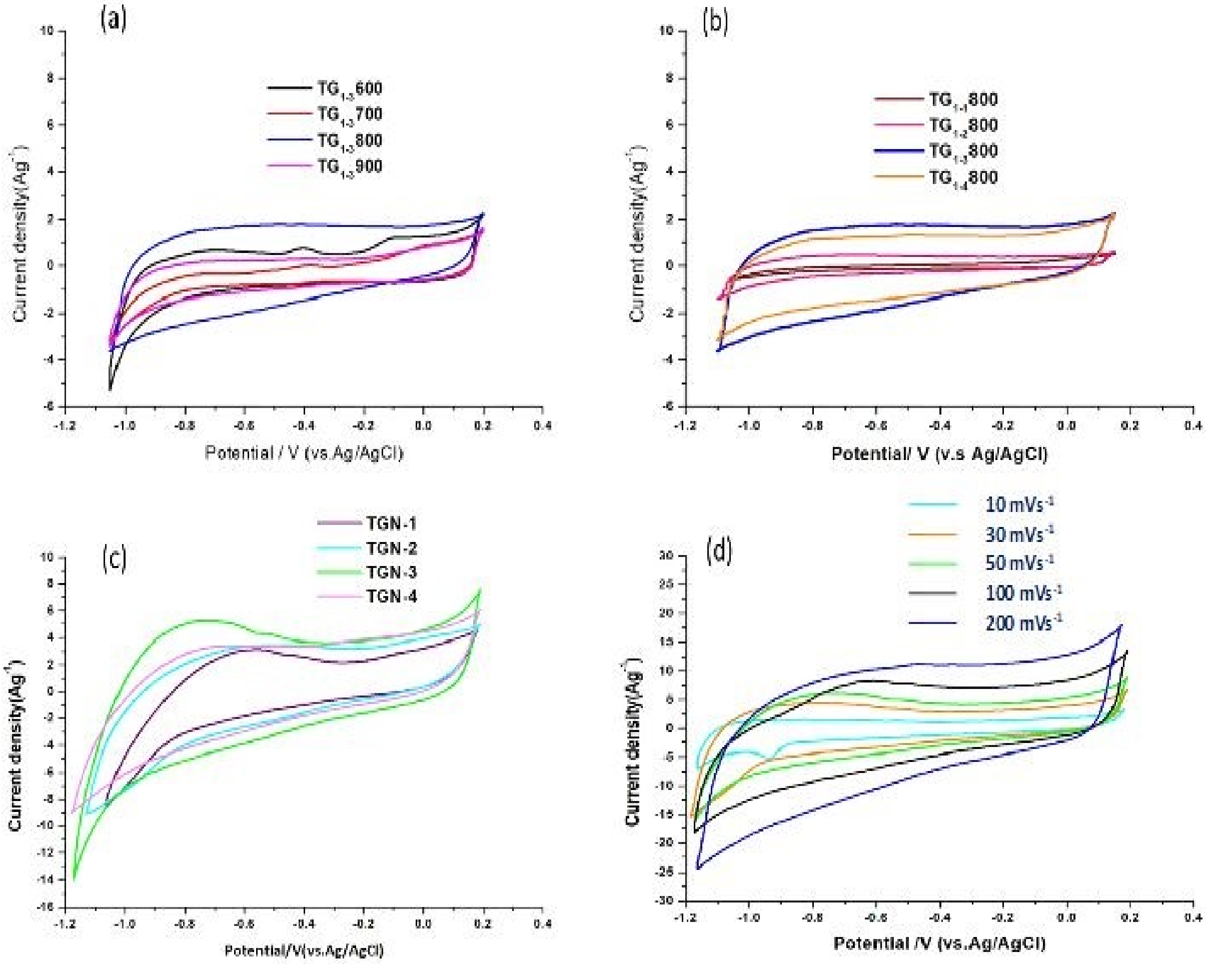

View Article Online
DOI: 10.1039/D5MA00328H

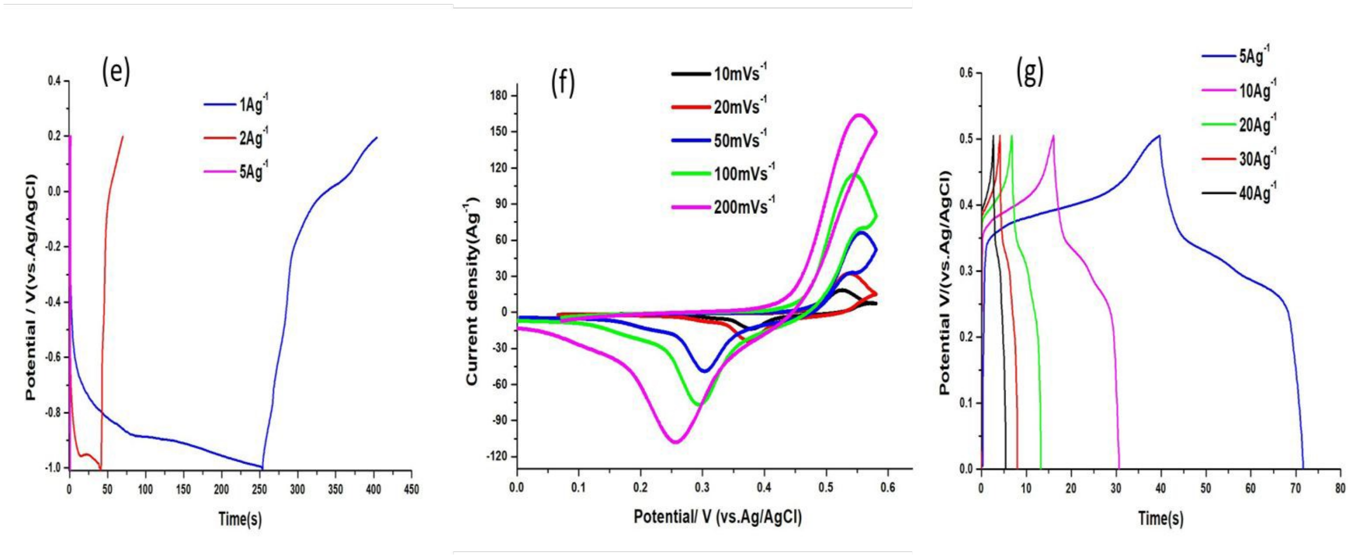

Fig.7. (a) Displays the comparison of CV curves for TG$_{1-3}$-600, TG$_{1-3}$-700, TG$_{1-3}$-800 and TG$_{1-3}$-900 measured at a scan rate of 50 mVs^{-1}. (b) displays the comparison of CV curves for TG$_{1-1}$-800, TG$_{1-2}$-800 , TG$_{1-3}$-800 , and TG$_{1-4}$-800 measured at a scan rate of 50m Vs^{-1} (c) displays the comparison of CV curves for TGN-1, TGN-2, TGN-3 , and TGN-4 measured at a scan rate of 50 mVs^{-1} (d) CV curves of TGN-3 at different scan rates. (e)Charge-Discharge curves of TGN-3 at different current densities. (f) CV curves of TGN-3 @Ni at different scan rates (g) Charge–discharge curves of TGN-3 @Ni at different current density

The EIS test was employed to evaluate the transport kinetics for electrochemical reaction process [42]. Each impedance spectrum consists of three main components: the intrinsic ohmic resistance (R_s), the interfacial charge transfer resistance (R_{ct}), and the Warburg diffusion resistance (R_w). R_s varies slightly with current density. In contrast, R_{ct} and R_w are related to ion diffusion in the electrolyte or at the electrolyte-electrode interface and are therefore sensitive to the shape and quality of the current density surface associated with the electrode as well as ion migration [57, 58]. The Nyquist plots of carbon samples which have been fitted by an equivalent circuit used at different temperatures are plotted in the support section (Fig. S2). The TG$_{1-3}$ − 600 , TG$_{1-3}$ − 700 , TG − 800 and TG$_{1-3}$ − 900 electrodes had respective Rs values of 0.43, 0.47, 0.47 and

View Article Online
DOI: 10.1039/D5MA00328H

0.43 Ω, and charge transfer resistances of 2991, 5759, 296.8 and 1686 Ω These findings suggest that the electrode resistance(R_{ct}) is decreased by activation at 800°C.

The disparity between the pore size distribution and the surface area difference in the carbon samples may be the reason of why the R_{ct} for $TG_{1-3}-800$ in the high frequency region of this fitting was lower than the R_{ct} for $TG_{1-3}-600$, $TG_{1-3}-700$ and $TG_{1-3}-900$. Furthermore, the carbon-containing electrode $TG_{1-3}-800$ mesoporous shape makes the pores more accessible. The sample $TG_{1-3}-800$ straight line slope is lower in the low frequency area, which could be because larger pores are more accessible than smaller ones at 800°C [59]. TGN-3's R_{ct} (2.5 Ω) is substantially lower than TG_{1-3}-800's R_{ct} (296.8 Ω) . This suggests that doping activated carbon with heteroatoms lowers the R_{ct}. This finding suggests that the electron conductivity is enhanced when functions containing nitrogen are added to the carbon matrix (Fig. S3). Remarkably, when doped with different ratios, the ratio of 1 to 3, or TGN-3, has a lower Warburg resistance in the mid-frequency zone and a smaller R_{ct} in the high-frequency region. At low frequencies, the slope of the straight line is also steeper. This suggests that the activated carbon doped with nitrogen (TGN-3) has diffusion resistance of the electrode material which is smaller and closer to the ideal capacitance behavior [14, 60, 61].

However, TGN-4's electronic conductivity decreases in comparison to TGN-3's due to an excess of defect sites in the conductive carbon framework caused by the overdose of urea (Fig. 8a)[62] .

Fig. 8b compares the Nyquist plots of impedance spectra for TGN-3 and TGN-3@Ni. The small R_{ct} appearance in the high-frequency region indicates that there is a lot of pore structure, particularly for mesopores and macropores, which have more pore accessibility than micropores [63]. The R_{ct} values for TGN-3 and TGN-3@Ni were predicted to be 2.54Ω and 5.57Ω, respectively,

View Article Online
DOI: 10.1039/D5MA00328H

with R_s values of about 0.32Ω and 0.3Ω, respectively. A lower Rs value often indicates more electrical conductivity. Apart from the effect of big pores, the inclusion of nickel oxide nanoparticles in TGN-3@Ni can assist boost the conductivity of the carbon matrix [63].The TGN-3 sample exhibits a tiny semicircle in the high-frequency area before transitioning to linearity in the low-frequency range. It shows that the electrode material's diffusion resistance is lower and closer to the optimum capacitance behaviour.

3.9. Electrochemical properties of the TGN-3@Ni // TGN-3 ASC device

To examine the practical use of TGN-3@Ni and TGN-3 electrodes, an asymmetric device is fabricated by pairing TGN-3@Ni and TGN-3 as the cathode and anode, respectively**.** With a potential window of 1.7 V, CV plots of the built TGN-3@Ni //TGN-3 device at several sweep speeds ranging from 10 to 100 mVs^{-1} are shown in Fig.8c. Because of the fast transport of electrons and diffusion of ions, the CV curves of the TGN-3@Ni//TGN-3 device show a large current response while maintaining their primary shape with regard to the excellent rate capability and reversibility, confirming an efficient charge storage behavior. To further assess electrochemical performance, GCD measurements were performed at current densities ranging from 1 Ag^{-1} to 10 Ag^{-1}, as shown in Fig. 8d. Each discharge line reveals that capacitance is mostly produced from plateaus from the faradaic process, which is consistent with the results of CV testing. The GCD curves retain an equilateral triangular shape, confirming the ASC's consistent capacitive performance [16, 53]. For the asymmetric supercapacitor, the mass-specific capacitance is calculated by the equation(4) [64]:

$$C_{ASC} = \frac{I.\Delta t}{M.\Delta V} \tag{4}$$

View Article Online
DOI: 10.1039/D5MA00328H

for ASC, M (g) means the total mass of active substances on two electrodes.

The specific energy (E, Wh/kg) and power (P, W/kg) were determined consistent with the galvanostatic data using the following equations (5,6):

$$E = \frac{1}{2} C_{ASC} \Delta V^2 \times \frac{1}{3.6} \tag{5}$$

$$P = 3600 \frac{E}{\Delta t} \tag{6}$$

where ΔV (V) is the cell voltage for charging and discharging [50] Fig. 8e compares the CV curves of TGN-3@Ni and TGN-3 electrode materials evaluated in a three-electrode setup at a scan rate of 30 mVs^{-1}.

The TGN-3@Ni electrode has a potential window of 0 to 0.56 V, whereas the TGN-3 electrode has a potential window of -1.18 to 0.2V. Thus, an operating voltage of 1.74 V is predicted from an ASC with the TGN-3@Ni as the positive electrode and the TGN-3 as the negative electrode, because the total two-electrode cell voltage is the sum of the potentials of the positive and negative electrodes [65].

The specific gravimetric capacitance of the asymmetric supercapacitor decreased with a fourfold increase in discharge current density (with 50.49% capacitance retention) because diffusion at high current densities impeded the migration of ions and OH^- within the electrode, resulting in low electrochemical utilization of electroactive materials (Fig.8f) [66].

Cyclic stability is an important feature of supercapacitors. As a result, the cycle stability of the TGN-3@Ni//TGN-3 device was studied by charging and discharging at 5 Ag^{-1} in Fig.8g. The specific capacitance of the TGN-3@Ni//TGN-3 device declines somewhat after 8000 cycles, but it retains 96.12% of its initial value, indicating outstanding recyclability. These results indicate

View Article Online
DOI: 10.1039/D5MA00328H

that choosing an appropriate strategy, including optimizing the carbon pore structure, incorporating heteroatoms, and combining carbon materials with metal oxides, is an effective strategy to significantly enhance their performance as supercapacitor electrode materials [67, 68].

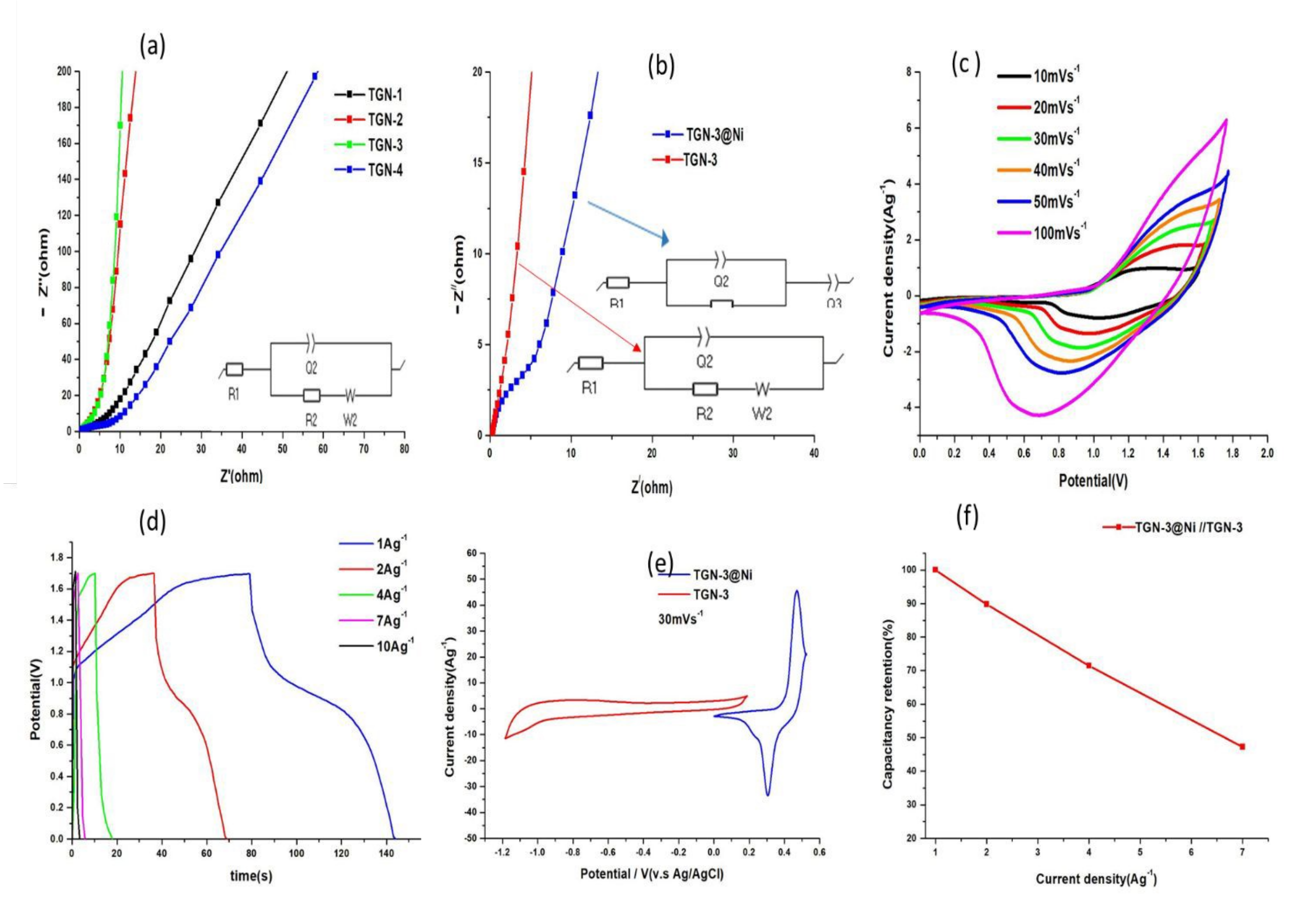

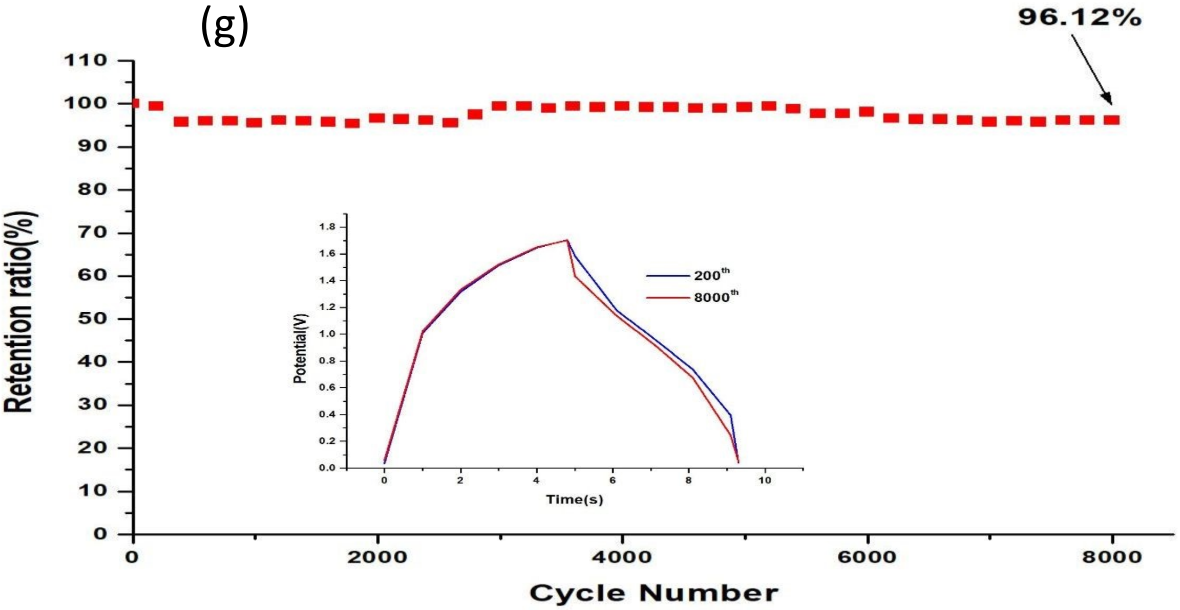

Fig.8. (a) displays the comparison of Nyquist plots for TGN-1, TGN-2, TGN-3and TGN-4 with frequency range of 0.01 Hz to100 kHz (b) Nyquist plots of electrodes TGN-3 and TGN-3@Ni (c) TGN-3@Ni//TGN-3asymmetric super capacitor device at different sweep rates in a 6 M KOH electrolyte (d) GCD curves of the assembled device at different current densities (e) Comparative CV curves of the TGN-3andTGN-3@Ni, tested in a three-electrode configuration at 30 mVs^{-1} (f) The gravimetric capacitance retention TGN-3@Ni//TGN-3 device as a function of the applied current density (g) Changes in the capacitance retention of the TGN-3@Ni//TGN-3 ASC as a function of cycle number

4. Conclusions

In summary, we successfully prepared a porous activated carbon doped with nitrogen derived from tragacanth gum at an optimized temperature of 800°C and an optimal 1:3 saturation ratio with $ZnCl_2$ as the activating agent and doped 1:3 with urea as the nitrogen source by a simple method for the first time. The resulting TGN-3 sample has a nitrogen content of 1.23 % and a high specific surface area of 3595.77 m^2g^{-1}. Also, the CV curve data and GCD results confirmed that the TGN-3 sample exhibited the best capacitive performance and capacitive behavior. Then, NiO nanoparticles were embedded in the TGN-3 carbon matrix using a hydrothermal method and

View Article Online
DOI: 10.1039/D5MA00328H

calcination process. This situation further reduces the internal and interfacial resistance of the matrix. The synergistic effect of these features in the TGN-3@Ni composite causes it to exhibit good electrical conductivity and excellent electrochemical performance. In a three-electrode setup, this electrode provides a specific capacity of 319.5 Fg^{-1} at a current density of 5 Ag^{-1}. In the same system, the TGN-3 electrode's specific capacity is 124.78 Fg^{-1} at a current density of 1 Ag^{-1} and the as-assembled TGN-3@Ni//TGN-3 may function at a stable electrochemical window up to 1.7 V and provide a high specific capacity of 40.06 Fg^{-1}. At a power density of 881.07 Wkg^{-1}, it can also provide a high energy density of 16.07 $Whkg^{-1}$. According to these findings, TGN-3@Ni composite shows promise as an electrode material for energy storage applications. Remarkably, other metals and metal oxides can be also tested in order to enhance the conductivity of TGN-3 and give a better performance to the end composite. Therefore, more study should be done in this field in the near future.

Data availability

The data that support the findings of this study are available on request from the corresponding author.

Conflicts of interest

There are no conflicts to declare.

Acknowledgements

The authors would like to acknowledge the Iran University of Science & Technology and Shahed university for sponsoring this work.

View Article Online
DOI: 10.1039/D5MA00328H

References

1. S. Ahmad, M. Ahmad, K. Manzoor, R. Purwar and S. Ikram, *International journal of biological macromolecules*, 2019, **136**, 870-890.
2. S. Tang, L. Jiang, Z. Jiang, Y. Ma, Y. Zhang and S. Su, *Polymers*, 2023, **15**, 2942.
3. E. N. Zare, P. Makvandi and F. R. Tay, *Carbohydrate polymers*, 2019, **212**, 450-467.
4. A. Scalia, P. Zaccagnini, M. Armandi, G. Latini, D. Versaci, V. Lanzio, A. Varzi, S. Passerini and A. Lamberti, *ChemSusChem*, 2021, **14**, 356-362.
5. Y. Lu, H. Zhou, W. Zhao, J. Jiang, J. Du and L. Zhao, *International Journal of Biological Macromolecules*, 2024, **282**, 137299.
6. M. Darroudi, Z. Sabouri, R. K. Oskuee, A. K. Zak, H. Kargar and M. H. N. Abd Hamid, *Ceramics International*, 2013, **39**, 9195-9199.
7. S. Taghavi Fardood, A. Ramazani and S. Joo, *Journal of Structural Chemistry*, 2018, **59**, 482-486.
8. M. K. Indana, B. R. Gangapuram, R. Dadigala, R. Bandi and V. Guttena, *Journal of Analytical Science and Technology*, 2016, **7**, 19.
9. S. Mallakpour and M. Okhovat, *International Journal of Biological Macromolecules*, 2021, **175**, 330-340.
10. Z. Guo, X. Han, C. Zhang, S. He, K. Liu, J. Hu, W. Yang, S. Jian, S. Jiang and G. Duan, *Chinese Chemical Letters*, 2024, **35**, 109007.
11. B. Chang, Y. Wang, K. Pei, S. Yang and X. Dong, *RSC Advances*, 2014, **4**, 40546-40552.
12. S. Sangon, K. Kotebantao, T. Suyala, Y. Ngernyen, A. J. Hunt and N. Supanchaiyamat, *Environmental Science: Water Research & Technology*, 2024, **10**, 1389-1405.
13. J. Su, Y. Xu, R. Yang, X. Lin, Y. Xie, H. Zhao, C. Shi, X. Dong, C. Wang and Y. Qing, *Colloids and Surfaces A: Physicochemical and Engineering Aspects*, 2024, **701**, 134964.
14. J. Chen, Y. Lin, J. Liu, D. Wu, X. Bai, D. Chen and H. Li, *Journal of Energy Storage*, 2021, **39**, 102640.
15. A. Querejeta-Fernandez, M. Parras, A. Varela, F. del Monte, M. Garcia-Hernandez and J. M. Gonzalez-Calbet, *Chemistry of Materials*, 2010, **22**, 6529-6541.
16. Y. Chen, R. Hu, J. Qi, Y. Sui, Y. He, Q. Meng, F. Wei and Y. Ren, *Materials Research Express*, 2019, **6**, 095605.
17. H. Chen, H. Wei, N. Fu, W. Qian, Y. Liu, H. Lin and S. Han, *Journal of Materials Science*, 2018, **53**, 2669-2684.
18. L. Ma, G. Sun, J. Ran, S. Lv, X. Shen and H. Tong, *ACS Applied Materials & Interfaces*, 2018, **10**, 22278-22290.
19. X. Jiang, S. Deng, J. Liu, N. Qi and Z. Chen, *Journal of Energy Storage*, 2021, **37**, 102426.
20. L. Sun, Y. Sun, Q. Fu and C. Pan, *Journal of Alloys and Compounds*, 2021, **888**, 161488.
21. L. Peng, Y. Liang, H. Dong, H. Hu, X. Zhao, Y. Cai, Y. Xiao, Y. Liu and M. Zheng, *Journal of power sources*, 2018, **377**, 151-160.
22. S. Liu, Y. Zhao, B. Zhang, H. Xia, J. Zhou, W. Xie and H. Li, *Journal of power sources*, 2018, **381**, 116-126.
23. Y. Yuan, R. Yi, Y. Sun, J. Zeng, J. Li, J. Hu, Y. Zhao, W. Sun, C. Zhao and L. Yang, *Journal of Nanomaterials*, 2018, **2018**, 7539509.
24. Y. Li, G. Wang, T. Wei, Z. Fan and P. Yan, *Nano energy*, 2016, **19**, 165-175.

View Article Online
DOI: 10.1039/D5MA00328H

25. Y. Hu, H. Liu, Q. Ke and J. Wang, *Journal of Materials Chemistry A*, 2014, **2**, 11753-11758.
26. H. Sayğılı and F. Güzel, *Journal of Cleaner Production*, 2016, **113**, 995-1004.
27. M. M. Baig, I. H. Gul, S. M. Baig and F. Shahzad, *Journal of Energy Storage*, 2021, **44**, 103370.
28. Y. Cui, H. Wang, X. Xu, Y. Lv, J. Shi, W. Liu, S. Chen and X. Wang, *Sustainable Energy & Fuels*, 2018, **2**, 381-391.
29. P. Li, C. Yang, C. Wu, Y. Wei, B. Jiang, Y. Jin and W. Wu, *Nanomaterials*, 2022, **12**, 2931.
30. I. Alali, A. U. Shehu and R. Mokaya, *Energy & Environmental Science*, 2024, **17**, 5024-5038.
31. J. Hou, K. Jiang, M. Tahir, X. Wu, F. Idrees, M. Shen and C. Cao, *Journal of Power Sources*, 2017, **371**, 148-155.
32. X. Wang, S. Yun, W. Fang, C. Zhang, X. Liang, Z. Lei and Z. Liu, *ACS Sustainable Chemistry & Engineering*, 2018, **6**, 11397-11407.
33. C. Zhang, F. Cui, Q. Ma and T. Cui, *Journal of Energy Storage*, 2024, **102**, 114150.
34. P. R. Kasturi, H. Ramasamy, D. Meyrick, Y. S. Lee and R. K. Selvan, *Journal of colloid and interface science*, 2019, **554**, 142-156.
35. Y. Lin, Z. Chen, C. Yu and W. Zhong, *Electrochimica Acta*, 2020, **334**, 135615.
36. P. Hao, Z. Zhao, J. Tian, H. Li, Y. Sang, G. Yu, H. Cai, H. Liu, C. Wong and A. Umar, *Nanoscale*, 2014, **6**, 12120-12129.
37. S. Ratso, I. Kruusenberg, M. Vikkisk, U. Joost, E. Shulga, I. Kink, T. Kallio and K. Tammeveski, *Carbon*, 2014, **73**, 361-370.
38. K. Zheng, Y. Li, M. Zhu, X. Yu, M. Zhang, L. Shi and J. Cheng, *Journal of Power Sources*, 2017, **366**, 270-277.
39. K. Wang, M. Xu, X. Wang, Z. Gu, Q. H. Fan, W. Gibbons and J. Croat, *RSC Advances*, 2017, **7**, 8236-8240.
40. S. C. Kishore, R. Atchudan, T. N. Jebakumar Immanuel Edison, S. Perumal, M. Alagan, R. Vinodh, M. Shanmugam and Y. R. Lee, *Energy & Fuels*, 2020, **34**, 14958-14967.
41. Y. Liu, X. Wang, X. Jiang, X. Li and L. Yu, *Nanoscale*, 2018, **10**, 22848-22860.
42. T. Liu, C. Jiang, B. Cheng, W. You and J. Yu, *Journal of Power Sources*, 2017, **359**, 371-378.
43. H. Chen, H. Wei, N. Fu, W. Qian, Y. Liu, H. Lin and S. Han, *Journal of Materials Science*, 2018, **53**, 2669-2684.
44. A. Noori, M. F. El-Kady, M. S. Rahmanifar, R. B. Kaner and M. F. Mousavi, *Chemical Society Reviews*, 2019, **48**, 1272-1341.
45. N. Choudhary, C. Li, J. Moore, N. Nagaiah, L. Zhai, Y. Jung and J. Thomas, *Advanced Materials*, 2017, **29**, 1605336.
46. R. Kumar, A. Soam and V. Sahajwalla, *Materials Advances*, 2020, **1**, 609-616.
47. C. Liu, Y. Hou, Y. Li and H. Xiao, *Journal of Colloid and Interface Science*, 2022, **614**, 566-573.
48. B. P. Bastakoti, H.-S. Huang, L.-C. Chen, K. C.-W. Wu and Y. Yamauchi, *Chemical communications*, 2012, **48**, 9150-9152.
49. J. Ji, L. L. Zhang, H. Ji, Y. Li, X. Zhao, X. Bai, X. Fan, F. Zhang and R. S. Ruoff, *ACS nano*, 2013, **7**, 6237-6243.

View Article Online
DOI: 10.1039/D5MA00328H

50. X. Li, J. Shen, W. Sun, X. Hong, R. Wang, X. Zhao and X. Yan, *Journal of Materials Chemistry A*, 2015, **3**, 13244-13253.
51. J. G. Ruiz-Montoya, L. V. Quispe-Garrido, J. C. Gómez, A. M. Baena-Moncada and J. M. Gonçalves, *Sustainable Energy & Fuels*, 2021, **5**, 5332-5365.
52. Y. Li, Q. Wei, R. Wang, J. Zhao, Z. Quan, T. Zhan, D. Li, J. Xu, H. Teng and W. Hou, *Journal of colloid and interface science*, 2020, **570**, 286-299.
53. X. Liu and F. Liu, *European Journal of Inorganic Chemistry*, 2018, **2018**, 987-991.
54. J. Pan, W. Zhong, Z. Gao, X. Yang, Y. Zhang, Y. Guan and X. Yan, *Ceramics International*, 2021, **47**, 27833-27842.
55. S. A. Al Kiey and M. S. Hasanin, *Environmental Science and Pollution Research*, 2021, **28**, 66888-66900.
56. X. Zhao, H. Chen, S. Wang, Q. Wu, N. Xia and F. Kong, *Materials Chemistry and Physics*, 2018, **215**, 157-162.
57. J. Zhao, Y. Jiang, H. Fan, M. Liu, O. Zhuo, X. Wang, Q. Wu, L. Yang, Y. Ma and Z. Hu, *Advanced Materials*, 2017, **29**, 1604569.
58. R. Ullah, N. Khan, R. Khattak, M. Khan, M. S. Khan and O. M. Ali, *Polymers*, 2022, **14**, 242.
59. J. Gamby, P. Taberna, P. Simon, J. Fauvarque and M. Chesneau, *Journal of power sources*, 2001, **101**, 109-116.
60. L. Sun, L. Wang, C. Tian, T. Tan, Y. Xie, K. Shi, M. Li and H. Fu, *Rsc Advances*, 2012, **2**, 4498-4506.
61. M. Y. Perdana, B. A. Johan, M. Abdallah, M. E. Hossain, M. A. Aziz, T. N. Baroud and Q. A. Drmosh, *The Chemical Record*, 2024, **24**, e202400007.
62. M. Chen, T. Le, Y. Zhou, F. Kang and Y. Yang, *ACS Applied Energy Materials*, 2020, **3**, 1653-1664.
63. Y. Hui, Y. Shewen, W. Yunfeng, Z. Jiaming, J. Jingwen, C. Jiahao, Z. Qinqin and L. Tongxiang, *Journal of Alloys and Compounds*, 2019, **792**, 976-982.
64. W. Hong, L. Wang, K. Liu, X. Han, Y. Zhou, P. Gao, R. Ding and E. Liu, *Journal of Alloys and Compounds*, 2018, **746**, 292-300.
65. H. Peng, C. Wei, K. Wang, T. Meng, G. Ma, Z. Lei and X. Gong, *ACS Applied Materials & Interfaces*, 2017, **9**, 17067-17075.
66. Z. Gao, W. Yang, J. Wang, N. Song and X. Li, *Nano Energy*, 2015, **13**, 306-317.
67. L. Wang, S. Chen, L. N. Bengoa, R. M. Gonzalez-Gil and P. Gomez-Romero, *Electrochimica Acta*, 2025, 146722.
68. X. Zhu, Y. Zeng, X. Zhao, D. Liu, W. Lei and S. Lu, *EcoEnergy*, 2025, e70000.

View Article Online
DOI: 10.1039/D5MA00328H

- The datasets supporting this article have been uploaded as part of the supplementary information.